Open Access

Catalysis Research

LIDSEN Publishing Inc.

Short Review

Perovskite Oxide Thermoelectric Module - A Way Forward

Abanti Nag *

Materials Science Division, CSIR - National Aerospace Laboratories, Bangalore, India; E-Mail: abanti@nal.res.in

* **Correspondence:** Abanti Nag; E-Mail: abanti@nal.res.in

Academic Editor: Wei Wang

Special Issue: Design and Development of Perovskite Materials for Energy Conversion Devices

Catalysis Research
2023, volume 3, issue 4
doi:10.21926/cr.2304024

Received: July 27, 2023
Accepted: October 07, 2023
Published: October 11, 2023

Abstract

In the era of renewable and sustainable energy, perovskite materials remain pioneers as energy harvesting materials, be it thermoelectric waste heat harvesting or photovoltaic solar cell application. Oxide perovskite material is an emerging thermoelectric material in solving energy shortage issues through waste heat recovery. The chemical and structural stabilities, oxidation resistance, and cost-effective and straightforward manufacturing process are a few advantages of the oxide-based thermoelectric materials. The perovskite thermoelectric materials and module thereof does not require any vacuum bagging for operation at high temperature, irrespective of the application environment. Perovskite $CaMnO_3$ displays a high Seebeck coefficient (S~-350 µV/K) due to correlated electron structure and low thermal conductivity (3 W m^{-1} K^{-1}) but high electrical resistivity simultaneously. The electrical resistivity of $CaMnO_3$ can be tuned by electron doping at the Ca-site and Mn-site. Electron doping by substituting Mn^{3+} with trivalent rare-earth ions increases the carrier concentration in the $CaMnO_3$ system by partially reducing Mn^{4+} to Mn^{3+}, improving electrical conductivity without altering the Seebeck coefficient. The dual-doped $Ca_{1-x}Yb_{x/2}Lu_{x/2}MnO_3$-based *n*-type perovskite thermoelectric material showed a much higher power factor than undoped $CaMnO_3$ and proved to be an efficient perovskite from the application point of view. The thermoelectric module, in combination with $CaMnO_3$ as an *n*-type element and $Ca_3Co_4O_9$ or

doped-$Ca_3Co_4O_9$ as the *p*-type element, is the most efficient device reported to date. The lab-scale power generation experiment is carried out for 4-element and 36-element modules consisting of perovskite $Ca_{1-x}Yb_{x/2}Lu_{x/2}MnO_3$ as *n*-type elements and $Ca_3Co_4O_9$ as *p*-type elements. The results showed the challenges of up-scaling the perovskite module for high-temperature waste heat harvesting applications.

Keywords
Perovskite oxide; thermoelectric module; power harvesting; waste heat

1. Introduction

Thermoelectric, as the word explains, represents the direct conversion of heat energy, waste heat, to electrical energy [1-3]. In the present scenario of continuous depletion of natural energy sources and the alarming situation of environmental pollution and global warming, there is a need for alternative sources of eco-friendly energy. Reducing waste heat to electricity is an option, as any industrial process generates lots of heat energy, which eventually goes wasted. Conventional systems for heat energy conversion, such as Rankine engines, involve moving parts that make them bulky and unsuitable for use in remote locations as they require constant maintenance. On the other hand, thermoelectric energy conversion using thermoelectric materials does not involve moving parts and, thereby, zero maintenance [4-6]. The word thermoelectric is a generic term for three related effects, viz. Seebeck result denotes voltage built-up in certain materials upon exposure to a temperature gradient, the Peltier effect describes heat absorption or release rate at materials junction on applying electric current, and the Thompson effect denotes a change in heat flux density of a material in a temperature gradient allowing current density to flows [7]. Thermoelectric energy harvesting involves the Seebeck effect, the principle of which was followed in simple devices such as thermocouples. The most prerequisite phenomenon of efficient thermoelectric energy harvesting is the thermoelectric materials used in the machine. A dimensionless quantity called the figure-of-merit (*ZT*) defines the performance of thermoelectric materials [8, 9]. A considerable Seebeck coefficient (α), high electrical conductivity (ρ), and low thermal conductivity (κ) result in maximum *ZT* according to the following relationship [10].

$$ZT = \frac{\alpha^2 \sigma}{\kappa} T \quad (1)$$

Now all the physical parameters defining *ZT* of thermoelectric material are functions of the charge carrier concentration of the materials; while electrical and thermal conductivity increases with charge carrier concentration, the Seebeck coefficient decreases. It is reported that to achieve maximum figure-of-merit, the optimal carrier concentration of the materials should be 10^{18}-10^{21} cm^{-3}, which falls under the category of heavily doped semiconductors [11, 12]. As Seebeck coefficient and thermal conductivity are temperature-dependent parameters, different materials have performance peaks at optimal temperature window, e.g., Bi-Te-based materials show *ZT* of 0.8-1.1 around 200°C [13, 14], Pb-Te-based alloys realize *ZT* of 1.2 between 200-600°C [15-20] and Si-Ge based alloys reach *ZT* of 0.5-0.9 above 600°C [21-23]. Other intermetallic alloys, such as

skutterudites, clathrates, and Heusler alloys, are also reported to show ZT values up to 1 [24, 25]. However, the aforesaid intermetallic alloys are primarily toxic and non-abundant, unstable in the open atmosphere, and thereby impact the cost and the durability of the thermoelectric module fabricated using intermetallic alloys. Unlike intermetallic alloys, transition metal oxide-based thermoelectric materials are more appropriate for high-temperature applications due to their inertness in chemical and oxidative environments [26-29]. However, metal oxides are considered inefficient entrants for thermoelectric applications because of high vibrational frequencies (high *k*) and low carrier mobility (high *r*) arising from highly polarized metal-oxygen ionic bonds with narrow orbital overlap and high bond energy. Only recently, the single crystal of Na_xCoO_2 has been reported with *ZT* close to unity, indicating oxide materials can be competitive with intermetallic alloys [30].

Waste heat recovery through thermoelectric materials requires the fabrication of a thermoelectric module device [31]. A thermoelectric module consists of *n*- and *p*-type materials in which electrons and holes participate in the conduction mechanism. Figure 1 shows the schematic of the thermoelectric module. Unlike traditional intermetallic alloys in which one material can be tuned to deliver both *n*- and *p*-type conduction, the conduction of metal oxides is uni-polar and arises mainly from an intrinsic defect. The *n*- and *p*-type elements are serially connected to flow electrically and vertically the heat from the hot zone to the cold zone to exhibit the conversion of heat energy to electricity in a thermoelectric module. The Seebeck voltage of individual legs gets added up, leading to the current flow through an external load resistance. The performance of the thermoelectric module depends on the hot (T_H) and cold (T_C) side temperatures it experiences, the temperature gradient (ΔT), and the *ZT* of the materials. Thus, the efficiency (η) of the thermoelectric module to convert heat (Q) into electrical power (P) can be represented as [10]:

$$\eta = \frac{\Delta T}{T_H} \times \frac{\sqrt{1 + Z_m T} - 1}{\sqrt{1 + Z_m T} + {T_C}/{T_H}} \tag{2}$$

where, $\Delta T = T_H - T_C$ and Z_m is the figure-of-merit of the module

$$Z_m = \frac{(S_n - S_p)}{(\rho_n + \rho_p)(\kappa_n + \kappa_p)} \tag{3}$$

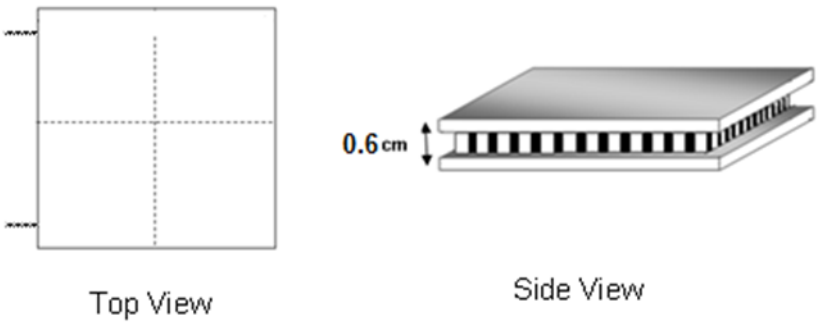

Figure 1 Single module configuration.

Therefore, the increased temperature gradient corresponds to the increased available heat for conversion following the Carnot efficiency. The literature has reported that a ZT ~ 1 is required for sufficient energy conversion (10%). To compete with the conventional heat pump, ZT ~ 3 is needed. As a rule of thumb, a thermocouple fabricated from thermoelectric materials with an average ZT of 1.5 would have an efficiency of 20% when operated at a temperature gradient of 500 K [8].

Thermoelectric can become competitive for small applications requiring less than 100 W because it is simple, compact, inexpensive, and easily scalable [32, 33]. There is an enormous demand for power harvesting at high temperatures to enable remote sensing technologies. Standalone wireless sensor systems operating at a high temperature require power supplies that can provide adequate power (at a level of 300-500 mW) for operation at a temperature of 500°C in an oxidizing environment. These systems do not exist presently. Therefore, this milestone is a stepping-stone towards developing higher power (1 W) systems with an ambient heat sink. This article summarizes an overview of recent progress on peroxide-based thermoelectric modules with an inclination towards the application in natural environments. An example module has been fabricated and tested to understand the future of perovskite-based thermoelectric modules.

2. Perovskite Oxide Thermoelectric Materials as n-Type Elements

Perovskite-oxides [34] is described by the general formula ABO_3, where 'A' can be rare earth, alkaline earth, alkali, and other large ions such as Pb^{2+} and Bi^{3+} and 'B' ions can be 3*d*, 4*d*, and 5*d* transitional metal ions. The perovskite $SrTiO_3$ and $CaMnO_3$ are the most promising *n*-type thermoelectric oxides.

Stoichiometric $SrTiO_3$ is isotropic cubic perovskite in which the 3d t_{2g} orbital of TiO_6 octahedron lies in the conduction band. The stoichiometric $SrTiO_3$ exhibits an insulating character with a band gap of 3.2 eV due to the d^0 configuration of Ti^{4+}. The semiconductor behavior of $SrTiO_3$ is experienced by doping at A and B-site as follows, where Ln and M represent the rare earth ions and transition metal ions, respectively [35]:

A-site:

$$Ln_2O_3 + 2BO_2 \rightarrow 2Ln_A + 2B_B^x + 2e' + 6O_O^x + \frac{1}{2}O_2 \uparrow \quad (4)$$

B-site:

$$2AO + M_2O_5 \rightarrow 2M_B + 2A_A^x + 2e' + 6O_O^x + \frac{1}{2}O_2 \uparrow \quad (5)$$

Electron doping shifts the Fermi energy from the forbidden band to the conduction band, making the system conductive through polaron formation. A-site substitution by La and B-site substitution by Nb are widely studied for $SrTiO_3$. A *ZT* of 0.27 at 1073 K is reported by Ohta et al. for La-doped $SrTiO_3$ single crystal [36]. The power factor of La-doped $SrTiO_3$ (28-36 mW cm^{-1} K^{-1}) is comparable to Bi_2Te_3; however, the high thermal conductivity of 9-12 W m^{-1} K^{-1} causes a low figure-of-merit in the system. Wang et al. reported suppression of thermal conductivity in mesoporous silica (MS)-$SrNb_{0.15}Ti_{0.85}O_3$ composites and Nb-doped $SrTiO_3$ with yttria (Y_2O_3) stabilized zirconia (YSZ) nano-precipitates through the formation of thermally insulating second

phase at grain boundaries [37]. The *ZT* values achieved were 0.165 and 0.2 at 900 K, respectively. Similarly, a high *ZT* of 0.33 at 900 K was reported for Nb-doped polycrystalline $SrTiO_3$ coated with surface-modified nano-sized titania (TiO_2) [38]. Park et al. carried out chemical colloidal synthesis accompanied by the SPS process to develop La-doped SrTiO3 with nano-grain that resulted in a *ZT* of 0.37 at 973 K [39]. Dehkordi et al. adopted a solid-state reaction and SPS technique to prepare $Sr_{0.85}Pr_{0.15}TiO_3$, resulting in a *ZT* of 0.35 [40]. Dy and La co-doped $SrTiO_3$ ($La_{0.08}Dy_{0.12}Sr_{0.8}TiO_3$) with nano-sized second phases lowered the thermal conductivity to 2.3 W m K^{-1} at 1074 K and showed *ZT* of 0.36 at 1048 K [41]. Zhang et al. reported a *ZT* of 0.40 in Nb-doped $SrTiO_3$, where oxygen vacancies are responsible for high electrical conductivity and low *ZT* [42]. However, the stability of the $SrTiO_3$-based compound is a concern due to the oxidation of TI to Ti^{4+} above 700 K in air, which results in insulating behavior [43].

On the other hand, $CaMnO_3$ is an orthorhombic perovskite-type structure that shows *G*-type anti-ferromagnetism and giant magnetoresistance. $CaMnO_3$ displays a high Seebeck coefficient (*S*~-350 mV/K) due to correlated electron structure and low thermal conductivity (3 W m^{-1} K^{-1}) but high electrical resistivity simultaneously [44-46]. Mn^{4+} ($3d^3$) in MnO_6 octahedron ($t_{2g}^3 e_g^0$) with negligible Jahn-Teller distortion primarily exhibits insulating character due to its e_g^0 state. Mn 3*d* states and O *p* states are accountable for electrical conductivity in the system. Electron doping at Ca-site and Mn-site increases the carrier concentration in the $CaMnO_3$ system by partially reducing Mn^{4+} to Mn^{3+}, improving electrical conductivity by a few orders of magnitude. Moreover, oxygen vacancies can also reduce Mn4+ to Mn3+, occupying e_g^0 state partially occupied. Electron-lattice interaction in the system creates a small polaron responsible for polaron hopping conduction for $CaMnO_3$. Further, formations of Mn^{3+} introduce Jahn-Teller distortion in the design, thereby reducing the thermal conductivity. The electron doping is experienced at Ca-site by rare-earth ions and Bi^{3+} and Mn-site Nb^{5+}, Ta^{5+}, Mo^{6+}, W^{6+}, etc [47-51]. Yb-doped $CaMnO_3$ shows a *ZT* of 0.16 at 1000 K, the highest among rare-earth doped $CaMnO_3$ [52]. Kabir et al. reported *ZT* of 0.25 at 973 K in Bi-doped $CaMnO_3$, where incorporating Bi improves electrical conductivity with marginal reduction of the Seebeck coefficient [53]. The highest *ZT* value reported for A-site doping is for dual-doped $Ca_{0.96}Dy_{0.02}Yb_{0.02}MnO_3$ with a *ZT* of 0.27 [54]. Among the B-site doped $CaMnO_3$, W-doped $CaMn_{0.96}W_{0.04}O_3$ exhibit *ZT* of 0.25 at 1225 K [55]. However, the highest *ZT* reported in the *n*-type $CaMnO_3$ system so far is Nb-doped $CaMn_{0.98}Nb_{0.02}O_3$ with a *ZT* of 0.3 [56].

Double perovskite-based oxide ($A_2B'B''O_6$) materials caught attention recently as thermoelectric (TE) materials due to their environment-friendly nature, high-temperature stability, better oxidation resistance, and lower processing cost compared to conventional chalcogenides and intermetallics with Ba_2CoNiO_6 results in a ZT around 0.8 at room temperature [57-61].

3. p-Type Element $Ca_3Co_4O_9$

$Ca_3Co_4O_9$ is "misfit layered" cobalt oxide with a modulated layered structure. The structure of $Ca_3Co_4O_9$ ($[Ca_2CoO_3]^{RS}[CoO_2]_{1.62}$) consists of a single CdI_2 type CoO_2 layer having CoO_6 octahedra interleaved with rock-salt- (RS-) type $[Ca_2CoO_3]$ layers [62]. The rock-salt layer controls the lattice thermal conductivity i.e., the in-plane thermal conductivity reduces with increasing rock-salt layers, keeping the electronic properties of the CoO_2 block unperturbed [63, 64]. The thermoelectric properties of misfit-layered oxide single crystals showed the most significant *ZT* = 1.2-2.7 for $Ca_3Co_4O_9$ at 873 K, and *ZT* ≥ 1.1 for $Bi_2Sr_2Co_2O_9$ at 1000 K [65, 66]. However, the strong anisotropy

in the thermoelectric parameters and the non-uniform crystal growth prevent the performance of the bulk compositions, resulting in a maximum *ZT* of 0.5 [67-70].

4. Perovskite Oxide-Based Thermoelectric Module

Perovskite $CaMnO_3$ is one the most widely explored *n*-type thermoelectric materials, and several researchers have investigated the power generation capabilities of $CaMnO_3$-based modules. Several groups have reported $CaMnO_3$-based oxide thermoelectric modules where doped and un-doped $CaMnO_3$ were used as *n*-type elements. Table 1 summarizes the perovskite $CaMnO_3$-based thermoelectric module reported in the literature based on power output [71-82]. The thermoelectric module, in combination with $CaMnO_3$ as an *n*-type element and $Ca_3Co_4O_9$ or doped-$Ca_3Co_4O_9$ as the *p*-type element, is the most efficient device reported to date. We have established that dual-doped $Ca_{1-x}Lu_{x/2}Yb_{x/2}MnO_3$ is one of the efficient *n*-type elements in the perovskite $CaMnO_3$ series. Similarly, $Ca_3Co_4O_9$ without any doping stands for efficient *p*-type material.

Table 1 The perovskite $CaMnO_3$-based thermoelectric module based on power output as reported in the literature.

Modules elements	p-n couples (pairs)	Elements Dimensions (mm^3)	P_{max} (mW)	V_{out} (V)	T_H (K)	ΔT (K)	Reference
n-$CaMnO_3$/p-$Ca_3Co_4O_9$	12	0.5 × 5 × 3	1.98	0.8	473	200	[71]
n-$Ca_{0.8}Dy_{0.2}MnO_3$/p-$Ca_{2.76}Cu_{0.24}Co_4O_9$	4 (π-shaped)	7 × 9 × 25	31.12	0.28	937	321	[72]
n-$Ca_{0.92}La_{0.08}MnO_3$/p-$Ca_{2.75}Gd_{0.25}Co_4O_9$	8 (fin type)	3 × 3 × 25	63.5	0.98	1046	390	[73]
n-$Ca_{0.9}Yb_{0.1}MnO_3$/p-$Ca_{2.7}Bi_{0.3}Co_4O_9$	1	3.5 × 3.5 × 5	137	0.226	1095	705	[74]
n-$Ca_{0.95}Sm_{0.05}MnO_3$/p-$Ca_3Co_4O_9$	2	4 × 4 × 5-10	31.5	0.4	1000	925	[75]
	2	4 × 4 × 35	31.5		990	630	[76]
n-$Ca_{0.98}Sm_{0.02}MnO_3$/p-$Ca_3Co_{4-x}Ag_xO_9$	2	3 × 6 × 6	36.8	0.32	973	523	[77]
n-$Ca_{0.98}Nb_{0.02}MnO_3$/p-$La_{1.98}Sr_{0.02}CuO_4$	2	4.5 × 4.5 × 4-10	88.8			622	[78]
n-$CaMn_{0.98}Nb_{0.02}O_3$/p-$GdCo_{0.95}Ni_{0.05}O_3$	2	4 × 4 × 5	40	0.35	800	500	[79]
n-$CaMn_{0.98}Mo_{0.02}O_3$/p-$Ca_{2.7}Bi_{0.3}Co_4O_9$	8	5 × 5 × 4.5	34	0.7	1273	975	[80]
n-$CaMnO_{3-\delta}$-$CaMn_2O_4$/p-$Ca_3Co_{4-x}O_{9+\delta}$	unicouple	Variable with hybrid junction	7.2	0.35	1173	650	[81]
n-$Ca_{0.99}Dy_{0.005}Lu_{0.005}MnO_3$/p-$Ca_3Co_4O_9$	7	5 × 5 × 5	7	0.34	773	200	[82]

5. Development of Materials

The powder sample of dual-doped *n*-$Ca_{1-x}Lu_{x/2}Yb_{x/2}MnO_3$ and *p*-$Ca_3Co_4O_9$ were prepared by the sol-gel methodology. The *n*-$Ca_{1-x}Lu_{x/2}Yb_{x/2}MnO_3$ powder samples were pressed in rectangular blocks and sintered at 1200°C for 5 h. Conversely, *p*-$Ca_3Co_4O_9$ powders were sintered through a hot-press technique at 1098 K and a pressure 25 MPa. The *n* and *p*-type rectangular blocks were diced into 3 mm × 3 mm × 5 mm cuboids to fabricate the thermoelectric module.

6. Fabrication of Thermoelectric Module

4-elements and 36-element thermoelectric modules were fabricated to study heat to electrical energy conversion in the lab level. The *n*-$Ca_{0.99}Lu_{0.005}Yb_{0.005}MnO_3$ and *p*-$Ca_3Co_4O_9$ elements were sandwiched alternately between insulating alumina plates of thickness 6 mm. The *n* and *p* connections were built between protecting alumina plates with silver plates and silver paint. One side of the alumina plate acted as a hot end, and the other side was the cold end. The hot end was attached to the heat source, and the output voltage was recorded from the cold end. The heat sink can be attached to the cold end. However, the lab scale experiment was carried out on a standalone module without attaching any heat sink.

7. Thermoelectric Power Generation [8]

The Seebeck, Peltier, Thompson, and Joule effects are the four basic physical phenomena governing thermoelectric generator operation. Mathematically, the energy flow through a unit volume under steady-state conditions is expressed as follows:

$$TJ\frac{dS}{dx} + \tau J\frac{dT}{dx} - \rho J^2 - \frac{d}{dx}\left(\kappa\frac{dT}{dx}\right) = 0 \tag{6}$$

where T = Temperature, J = electrical current density, S = Seebeck coefficient, τ = Thompson coefficient, ρ = electrical resistivity, and κ = thermal conductivity of the materials. Considering the negligible Thompson effect (as explained in Ref. 8, Chapter 2), the heat flow at the hot side is (where I is the current flow) can be represented as:

$$\begin{aligned} Q_h &= \left[S_{TEG}T_H I + K_{TEG}(T_H - T_C) - \frac{1}{2}I^2R_{TEG}\right] \\ &= \left[\left(S_p + S_n\right)T_H I + \left(K_p + K_n\right)(T_H - T_C) - \frac{1}{2}I^2\left(R_p + R_n + R_{contact}\right)\right] \end{aligned} \tag{7}$$

Similarly, the heat flow from the cold side can be represented as:

$$\begin{aligned} Q_c &= \left[S_{TEG}T_H I + K_{TEG}(T_H - T_C) + \frac{1}{2}I^2R_{TEG}\right] \\ &= \left[\left(S_p + S_n\right)T_H I + \left(K_p + K_n\right)(T_H - T_C) + \frac{1}{2}I^2\left(R_p + R_n + R_{contact}\right)\right] \end{aligned} \tag{8}$$

The resistance of the module (R_{TEG}) is collected form of the resistance of *n*-element (R_n), *p*-element (R_p), and the contact resistance ($R_{contact}$).

Together, the power produced by the module (P_{TEG}) can be represented as:

$$P_{TEG} = Q_H - Q_C = S_{TEG}(T_H - T_C)I - I^2R_{TEG} \quad (9)$$

A voltage of the module:

$$V_{TEG} = S_{TEG}(T_H - T_C) - IR_{TEG} \quad (10)$$

8. Power Output Analyses of Fabricated 4-Elements TE Module

The lab-scale testing was initially undertaken on the fabricated 4-element TE module. A hot plate was used for this purpose. The hot side of the module was kept on a hot plate, and the temperature of the hot-plate was raised to 773 K with a uniform heating rate. Open-circuit voltage was measured on the module's cold side during the heating-up process. To measure the output voltage, the Pt-lead wires were attached to the module's cold side. The output voltage was recorded by a digital multimeter-data acquisition system in the open air without any coolant to understand the module's performance in standalone conditions. The four-probe Delta mode technique measured the module resistance, including internal and contact resistance. The voltage terminals were attached to the same position behind the current airports to measure the resistance. Figure 2 shows the power generation properties of the 4-element module. The I-V characteristics showed a maximum intercept at 0.212 V with the hot-side temperature (T_H) of 773 K at open air (Figure 2a). The P-V plot showed that the full power achieved was 11 mW (Figure 2b). Figures 2c and 2d show the variation of open circuit voltage, closed circuit voltage (I = 20 mA), and powder output with varying temperatures. The power obtained under a closed circuit is 4 mW at 500°C.

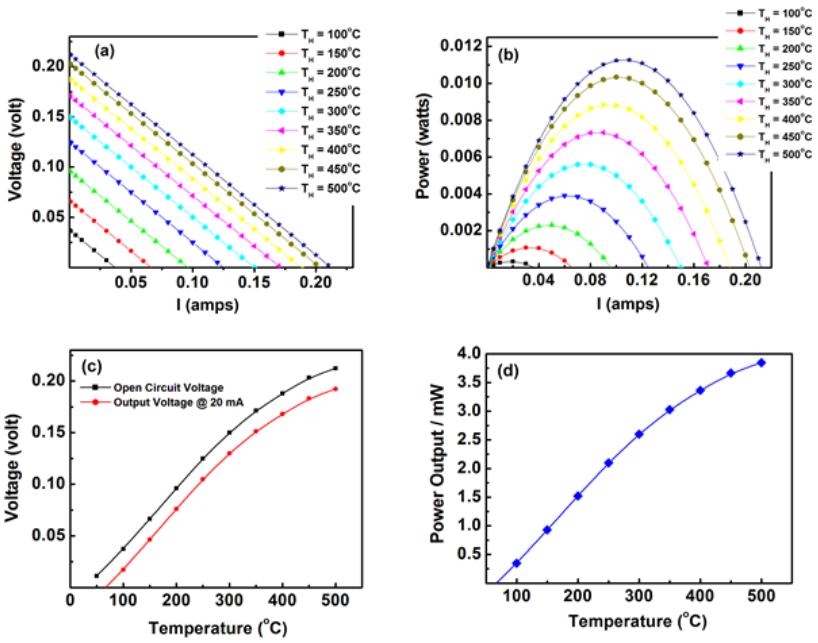

Figure 2 Calculated (a) module voltage and (b) module power output of fabricated 4-element thermoelectric module under various hot-source temperatures. (c) Open circuit voltage and output voltage calculated at 20 mA current flow and (d) power output with temperature variation.

9. Power Output Analyses of Fabricated 36-Elements TE Module

To understand how scaling up affects the power generation characteristics of the thermoelectric module, the 36-elements module was fabricated similarly with each element dimension of 3 mm × 3 mm × 5 mm. The module was tested under the same conditions as of 4-elements module. Figure 3 shows the power generation properties of a 36-elements module with hot-side temperatures up to 500°C. The *I-V* plot conducted a maximum intercept at 0.85 Volt with a hot-side temperature (T_H) of 500°C where the other side has been experiencing the open-air atmosphere (Figure 3a). The *P-V* characteristics showed that the maximum power obtained under this condition is up to 18 mW (Figure 3b). Figures 3c and 3d showed the variation of open circuit voltage, closed circuit voltage (I = 20 mA), and powder output with varying temperatures. The power obtained under a closed circuit is 13 mW at 500°C.

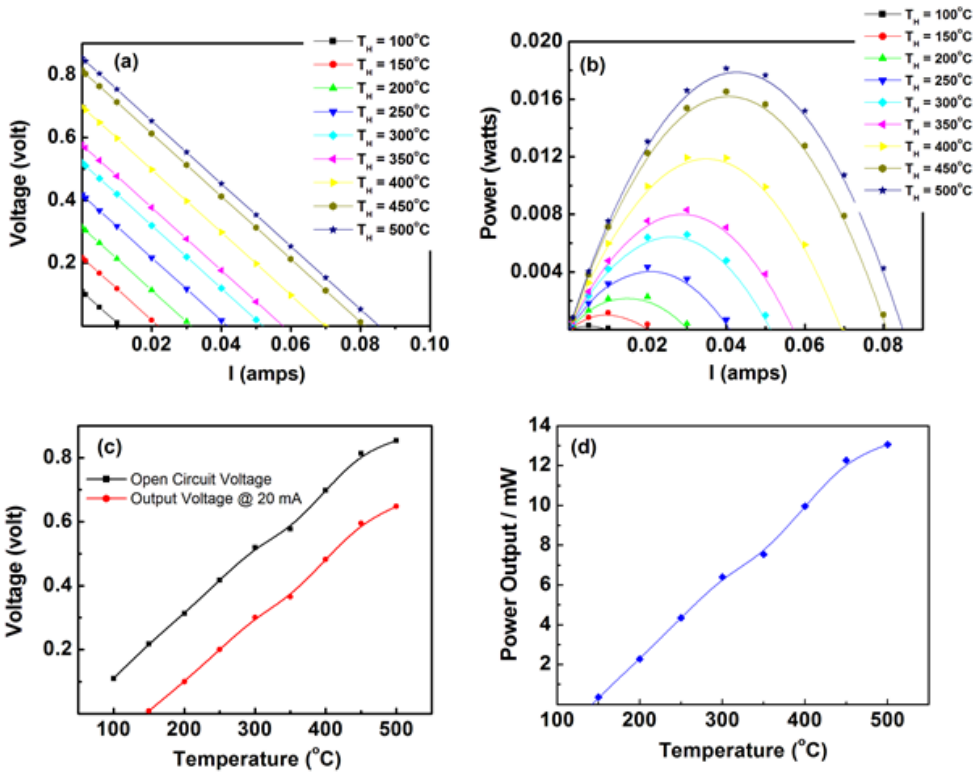

Figure 3 Calculated (a) module voltage and (b) module power output of fabricated 4-element thermoelectric module under various hot-source temperatures. (c) Open circuit voltage and output voltage calculated at 20 mA current flow and (d) power output with temperature variation.

10. Challenges and Future Directions

There were a lot of challenges on thermoelectric modules that need to be addressed for efficient transformation of heat to electricity. The significant advantage is that the figure-of-merit of thermoelectric materials gets halved in the module figure-of-merit due to parasitic losses such as thermal and electrical resistance at the contact points and thermal losses from the side of the thermoelectric elements. Therefore, the fabrication of the module to reduce the heat losses on the one hand and overcome the contact resistance on the other are the daunting tasks to achieve

the maximum performance from the thermoelectric module. Thus, the materials development to obtain high ZT alone cannot solve the practical problem of applying thermoelectric materials. Engineering thermoelectric modules with nominal heat loss and contact resistance is one of the aspects of futuristic device technology.

Acknowledgments

The author thanks Council of Scientific and Industrial Research and National Aerospace Laboratories for financial support.

Author Contributions

The author did all the research work of this study.

Competing Interests

The author has declared that no competing interests exist.

References

1. DiSalvo FJ. Thermoelectric cooling and power generation. Science. 1999; 285: 703-706.
2. Bell LE. Cooling, heating, generating power, and recovering waste heat with thermoelectric systems. Science. 2008; 321: 1457-1461.
3. Xiao Y, Zhao LD. Seeking new, highly effective thermoelectrics. Science. 2020; 367: 1196-1197.
4. Snyder GJ, Toberer ES. Complex thermoelectric materials. Nat Mater. 2008; 7: 105-114.
5. Tritt TM. Recent Trends in Thermoelectric Materials Research I & II. Semiconductors and semimetals. Cambridge, MA, US: Academic Press; 2001.
6. Massetti M, Jiao F, Ferguson AJ, Zhao D, Wijeratne K, Würger A, et al. Unconventional thermoelectric materials for energy harvesting and sensing applications. Chem Rev. 2021; 121: 12465-12547.
7. Kozinsky B, Singh DJ. Thermoelectrics by computational design: Progress and opportunities. Annu Rev Mater Res. 2021; 51: 565-590.
8. Rowe DM. Thermoelectrics Handbook: Macro to Nano. Boca Raton, FL, US: CRC Press; 2006.
9. Ismail BI, Ahmed WH. Thermoelectric power generation using waste-heat energy as an alternative green technology. Recent Pat Electr Electron Eng. 2009; 2: 27-39.
10. Snyder GJ. Small thermoelectric generators. Electrochem Soc Interface. 2008; 17: 54.
11. Chen L, Liu R, Shi X. Thermoelectric materials and devices. Amsterdam, Netherlands: Elsevier; 2020.
12. Finn PA, Asker C, Wan K, Bilotti E, Fenwick O, Nielsen CB. Thermoelectric materials: Current status and future challenges. Front Electron Mater. 2021; 1: 677845.
13. Nozariasbmarz A, Poudel B, Li W, Kang HB, Zhu H, Priya S. Bismuth telluride thermoelectrics with 8% module efficiency for waste heat recovery application. Iscience. 2020; 23: 101340.
14. Jia F, Yin X, Cheng WW, Lan JT, Zhan SH, Chen L, et al. Room-temperature high-performance thermoelectric $Bi_{0.6}Sb_{0.4}Te$: Elimination of detrimental band inversion in BiTe. Angew Chem. 2023; 135: e202218019.

15. Xiao Y, Zhao LD. Charge and phonon transport in PbTe-based thermoelectric materials. NPJ Quantum Mater. 2018; 3: 55.
16. Hao X, Chen X, Zhou X, Zhang L, Tao J, Wang C, et al. Performance optimization for PbTe-based thermoelectric materials. Front Energy Res. 2021; 9: 754532.
17. Shi D, Lam KH. Enhanced thermoelectric properties of $PbTe_{0.95}$ via N-type PbS nano-inclusions using a conventional sintering method. J Mater Chem C. 2021; 9: 15977-15982.
18. Lee J, Choo S, Ju H, Hong J, Yang SE, Kim F, et al. Doping-induced viscoelasticity in PbTe thermoelectric inks for 3D printing of power-generating tubes. Adv Energy Mater. 2021; 11: 2100190.
19. Liu M, Zhang X, Wu Y, Bu Z, Chen Z, Li W, et al. Screening metal electrodes for thermoelectric PbTe. ACS Appl Mater Interfaces. 2023; 15: 6169-6176.
20. Wu H, Shi XL, Duan J, Liu Q, Chen ZG. Advances in Ag_2Se-based thermoelectrics from materials to applications. Energy Environ Sci. 2023; 16: 1870-1906.
21. Li Y, Wang G, Akbari Saatlu M, Procek M, Radamson HH. Si and SiGe nanowire for micro-thermoelectric generator: A review of the current state of the art. Front Mater. 2021; 8: 611078.
22. Basu R, Singh A. High temperature Si-Ge alloy towards thermoelectric applications: A comprehensive review. Mater Today Phys. 2021; 21: 100468.
23. Ozawa T, Murata M, Suemasu T, Toko K. Flexible thermoelectric generator based on polycrystalline SiGe thin films. Materials. 2022; 15: 608.
24. Gonçalves AP, Godart C. New promising bulk thermoelectrics: Intermetallics, pnictides and chalcogenides. Eur Phys J B. 2014; 87: 42.
25. Rogl G, Rogl PF. Development of thermoelectric half-Heusler alloys over the past 25 years. Crystals. 2023; 13: 1152.
26. Nag A, Shubha V. Oxide thermoelectric materials: A structure-property relationship. J Electron Mater. 2014; 43: 962-977.
27. Prasad R, Bhame SD. Review on texturization effects in thermoelectric oxides. Mater Renewable Sustainable Energy. 2020; 9: 3.
28. Peng L, Miao N, Wang G, Zhou J, Elliott SR, Sun Z. Novel metal oxides with promising high-temperature thermoelectric performance. J Mater Chem C. 2021; 9: 12884-12894.
29. Zhang P, Lou Z, Gong L, Wu Z, Chen X, Xu W, et al. Development and applications of thermoelectric oxide ceramics and devices. Energies. 2023; 16: 4475.
30. Terasaki I, Sasago Y, Uchinokura K. Large thermoelectric power in $NaCo_2O_4$ single crystals. Phys Rev B. 1997; 56: R12685.
31. Merkulov OV, Lopes D, Markov AA, Ferreira NM, Patrakeev MV, Kovalevsky AV. Tubular thermoelectric module based on oxide elements grown by the laser floating zone. ACS Appl Energy Mater. 2021; 4: 5848-5857.
32. Yadav S, Sharma P, Yamasani P, Minaev S, Kumar S. A prototype micro-thermoelectric power generator for micro-electromechanical systems. Appl Phys Lett. 2014; 104: 123903.
33. Chen J, Klein J, Wu Y, Xing S, Flammang R, Heibel M, et al. A thermoelectric energy harvesting system for powering wireless sensors in nuclear power plants. IEEE Trans Nucl Sci. 2016; 63: 2738-2746.
34. Mitchell RH. Perovskites: Modern and Ancient. Ontario, Canada: Almaz Press; 2002.

35. Koumoto K, Wang Y, Zhang R, Kosuga A, Funahashi R. Oxide thermoelectric materials: A nanostructuring approach. Annu Rev Mater Res. 2010; 40: 363-394.
36. Muta H, Kurosaki K, Yamanaka S. Thermoelectric properties of reduced and La-doped single-crystalline $SrTiO_3$. J Alloys Compd. 2005; 392: 306-309.
37. Wang N, Chen H, He H, Norimatsu W, Kusunoki M, Koumoto K. Enhanced thermoelectric performance of Nb-doped $SrTiO_3$ by nano-inclusion with low thermal conductivity. Sci Rep. 2013; 3: 3449.
38. Li E, Wang N, He H, Chen H. Improved thermoelectric performances of $SrTiO_3$ ceramic doped with Nb by surface modification of nanosized titania. Nanoscale Res Lett. 2016; 11: 188.
39. Park K, Son JS, Woo SI, Shin K, Oh MW, Park SD, et al. Colloidal synthesis and thermoelectric properties of La-doped $SrTiO_3$ nanoparticles. J Mater Chem A. 2014; 2: 4217-4224.
40. Mehdizadeh Dehkordi A, Bhattacharya S, Darroudi T, Graff JW, Schwingenschlögl U, Alshareef HN, et al. Large thermoelectric power factor in Pr-doped $SrTiO_{3-\delta}$ ceramics via grain-boundary-induced mobility enhancement. Chem Mater. 2014; 26: 2478-2485.
41. Wang HC, Wang CL, Su WB, Liu J, Sun Y, Peng H, et al. Doping effect of La and Dy on the thermoelectric properties of $SrTiO_3$. J Am Ceram Soc. 2011; 94: 838-842.
42. Blennow P, Hagen A, Hansen KK, Wallenberg LR, Mogensen M. Defect and electrical transport properties of Nb-doped $SrTiO_3$. Solid State Ion. 2008; 179: 2047-2058.
43. Shi XL, Wu H, Liu Q, Zhou W, Lu S, Shao Z, et al. $SrTiO_3$-based thermoelectrics: Progress and challenges. Nano Energy. 2020; 78: 105195.
44. Zeng Z, Greenblatt M, Croft M. Large magnetoresistance in antiferromagnetic $CaMnO_{3-\delta}$. Phys Rev B. 1999; 59: 8784.
45. Marsh DB, Parris PE. High-temperature thermopower of $LaMnO_3$ and related systems. Phys Rev B. 1996; 54: 16602.
46. Wang Y, Sui Y, Cheng J, Wang X, Lu Z, Su W. High temperature metal-insulator transition induced by rare-earth doping in perovskite $CaMnO_3$. J Phys Chem C. 2009; 113: 12509-12516.
47. Bose RS, Nag A. Investigation of thermoelectric performance and power generation characteristics of dual-doped $Ca_{1-x}RE'_{x/2}RE''_{x/2}MnO_3$ (RE′/RE″ = Dy, Gd, Yb, Lu; $0.05 \leq x \leq 0.1$). ACS Appl Energy Mater. 2018; 1: 3151-3158.
48. Bose RS, Nag A. Defect-Associated thermoelectric transport properties of dual-substituted $CaMn_{1-x}Nb_{x/2}M_{x/2}O_3$ (M = Mo, W; $0.02 \leq x \leq 0.06$). J Electron Mater. 2017; 46: 6653-6661.
49. Bose RS, Nag A. High temperature transport properties of co-substituted $Ca_{1-x}Ln_xMn_{1-x}Nb_xO_3$ (Ln = Yb, Lu; $0.02 \leq x \leq 0.08$). Mater Res Bull. 2016; 74: 41-49.
50. Bose RS, Nag A. Effect of dual-doping on the thermoelectric transport properties of $CaMn_{1-x}Nb_{x/2}Ta_{x/2}O_3$. RSC Adv. 2016; 6: 52318-52325.
51. Nag A, D'Sa F, Shubha V. Doping induced high temperature transport properties of $Ca_{1-x}Gd_xMn_{1-x}Nb_xO_3$ ($0 \leq x \leq 0.1$). Mater Chem Phys. 2015; 151: 119-125.
52. Flahaut D, Mihara T, Funahashi R, Nabeshima N, Lee K, Ohta H, et al. Thermoelectrical properties of A-site substituted $Ca_{1-x}Re_xMnO_3$ system. J Appl Phys. 2006; 100: 084911.
53. Kabir R, Tian R, Zhang T, Donelson R, Tan TT, Li S. Role of Bi doping in thermoelectric properties of $CaMnO_3$. J Alloys Compd. 2015; 628: 347-351.

54. Zhu Y, Wang C, Su W, Liu J, Li J, Zhang X, et al. Influence of rare-earth elements doping on thermoelectric properties of $Ca_{0.98}Dy_{0.02}MnO_3$ at high temperature. J Solid State Chem. 2015; 225: 105-109.
55. Kabir R, Zhang T, Wang D, Donelson R, Tian R, Tan TT, et al. Improvement in the thermoelectric properties of $CaMnO_3$ perovskites by W doping. J Mater Sci. 2014; 49: 7522-7528.
56. Bocher L, Aguirre MH, Logvinovich D, Shkabko A, Robert R, Trottmann M, et al. $CaMn_{1-x}Nb_xO_3$ ($x \leq 0.08$) perovskite-type phases as promising new high-temperature n-type thermoelectric materials. Inorg Chem. 2008; 47: 8077-8085.
57. Maiti T, Saxena M, Roy P. Double perovskite ($Sr_2B'B''O_6$) oxides for high-temperature thermoelectric power generation-A review. J Mater Res. 2019; 34: 107-125.
58. Rahman AU, Aurangzeb M, Khan R, Zhang Q, Dahshan A. Predicted double perovskite material $CaZrTiO_6$ with enhanced n-type thermoelectric performance. J Solid State Chem. 2022; 305: 122661.
59. Mir SA, Gupta DC. Scrutinizing the stability and exploring the dependence of thermoelectric properties on band structure of 3d-3d metal-based double perovskites Ba_2FeNiO_6 and Ba_2CoNiO_6. Sci Rep. 2021; 11: 10506.
60. Wu H, Shi XL, Liu WD, Li M, Gao H, Zhou W, et al. Double perovskite Pr_2CoFeO_6 thermoelectric oxide: Roles of Sr-doping and Micro/nanostructuring. Chem Eng J. 2021; 425: 130668.
61. Wu H, Shi XL, Liu WD, Gao H, Wang DZ, Yin LC, et al. Ni doping and rational annealing boost thermoelectric performance of nanostructured double perovskite $Pr_{1.8}Sr_{0.2}CoFeO_6$. Appl Mater Today. 2022; 29: 101580.
62. Lambert S, Leligny H, Grebille D. Three forms of the misfit layered cobaltite $[Ca_2CoO_3][CoO_2]_{1.62}$ A 4D structural investigation. J Solid State Chem. 2001; 160: 322-331.
63. Wu L, Meng Q, Jooss C, Zheng JC, Inada H, Su D, et al. Origin of phonon glass-electron crystal behavior in thermoelectric layered cobaltate. Adv Funct Mater. 2013; 23: 5728-5736.
64. Terasaki I, Tanaka H, Satake A, Okada S, Fujii T. Out-of-plane thermal conductivity of the layered thermoelectric oxide $Bi_{2-x}Pb_xSr_2Co_2O_y$. Phys Rev B. 2004; 70: 214106.
65. Funahashi R, Matsubara I, Ikuta H, Takeuchi T, Mizutani U, Sodeoka S. An oxide single crystal with high thermoelectric performance in air. Jpn J Appl Phys. 2000; 39: L1127.
66. Funahashi R, Shikano M. $Bi_2Sr_2Co_2O_y$ whiskers with high thermoelectric figure of merit. Appl Phys Lett. 2002; 81: 1459-1461.
67. Li S, Funahashi R, Matsubara I, Ueno K, Sodeoka S, Yamada H. Synthesis and thermoelectric properties of the new oxide materials $Ca_{3-x}Bi_xCo_4O_{9+\delta}$ ($0.0 < x < 0.75$). Chem Mater. 2000; 12: 2424-2427.
68. Wang Y, Sui Y, Cheng J, Wang X, Su W. Comparison of the high temperature thermoelectric properties for Ag-doped and Ag-added $Ca_3Co_4O_9$. J Alloys Compd. 2009; 477: 817-821.
69. Van Nong N, Pryds N, Linderoth S, Ohtaki M. Enhancement of the thermoelectric performance of p-type layered oxide $Ca_3Co_4O_{(9+\delta)}$ through heavy doping and metallic nanoinclusions. Adv Mater. 2011; 23: 2484-2490.
70. Nong NV, Yanagiya S, Monica S, Pryds N, Ohtaki M. High-temperature thermoelectric and microstructural characteristics of cobalt-based oxides with Ga substituted on the Co-site. J Electron Mater. 2011; 40: 716-722.

71. Seetawan T, Singsoog K, Srichai S, Thanachayanont C, Amornkitbamrung V, Chindaprasirt P. Thermoelectric energy conversion of p-$Ca_3Co_4O_9$/n-$CaMnO_3$ module. Energy Procedia. 2014; 61: 1067-1070.
72. Park K, Lee GW. Fabrication and thermoelectric power of π-shaped $Ca_3Co_4O_9$/$CaMnO_3$ modules for renewable energy conversion. Energy. 2013; 60: 87-93.
73. Matsubara I, Funahashi R, Takeuchi T, Sodeoka S, Shimizu T, Ueno K. Fabrication of an all-oxide thermoelectric power generator. Appl Phys Lett. 2001; 78: 3627-3629.
74. Kosuga A, Wang Y, Yubuta K, Koumoto K, Funahashi R. Thermoelectric properties of polycrystalline $Ca_{0.9}Yb_{0.1}MnO_3$ prepared from nanopowder obtained by gas-phase reaction and its application to thermoelectric power devices. Jpn J Appl Phys. 2010; 49: 071101.
75. Reddy ES, Noudem JG, Hebert S, Goupil C. Fabrication and properties of four-leg oxide thermoelectric modules. J Phys D Appl Phys. 2005; 38: 3751.
76. Noudem JG, Lemonnier S, Prevel M, Reddy ES, Guilmeau E, Goupil C. Thermoelectric ceramics for generators. J Eur Ceram Soc. 2008; 28: 41-48.
77. Han L, Jiang Y, Li S, Su H, Lan X, Qin K, et al. High temperature thermoelectric properties and energy transfer devices of $Ca_3Co_{4-x}Ag_xO_9$ and $Ca_{1-y}Sm_yMnO_3$. J Alloys Compd. 2011; 509: 8970-8977.
78. Tomeš P, Trottmann M, Suter C, Aguirre MH, Steinfeld A, Haueter P, et al. Thermoelectric oxide modules (TOMs) for the direct conversion of simulated solar radiation into electrical energy. Materials. 2010; 3: 2801-2814.
79. Tomeš P, Robert R, Trottmann M, Bocher L, Aguirre MH, Bitschi A, et al. Synthesis and characterization of new ceramic thermoelectrics implemented in a thermoelectric oxide module. J Electron Mater. 2010; 39: 1696-1703.
80. Urata S, Funahashi R, Mihara T, Kosuga A, Sodeoka S, Tanaka T. Power generation of a p-type $Ca_3Co_4O_9$/n-type $CaMnO_3$ module. Int J Appl Ceram Technol. 2007; 4: 535-540.
81. Kanas N, Bjørk R, Wells KH, Schuler R, Einarsrud MA, Pryds N, et al. Time-enhanced performance of oxide thermoelectric modules based on a hybrid p-n junction. ACS Omega. 2020; 6: 197-205.
82. Nag A, Sathiyamoorthy K. An energy harvesting perspective of a perovskite based thermoelectric module: Fabrication and evaluation. J Electron Mater. 2020; 49: 7036-7043.